



Quasi-simultaneous *INTEGRAL*, *SWIFT*, and *NuSTAR* Observations of the New X-Ray Clocked Burster 1RXS J180408.9-342058

M. Fiocchi¹ , A. Bazzano¹ , G. Bruni¹ , R. Ludlam^{2,3} , L. Natalucci¹ , F. Onori¹, and P. Ubertini¹

¹ Istituto di Astrofisica e Planetologia Spaziali -INAF- Via Fosso del Cavaliere 100, Roma, I-00133, Italy

² Cahill Center for Astronomy and Astrophysics, California Institute of Technology, Pasadena, CA 91125, USA

Received 2017 June 1; revised 2019 October 10; accepted 2019 October 11; published 2019 December 6

Abstract

We report the quasi-simultaneous *INTEGRAL*, *SWIFT*, and *NuSTAR* observations showing spectral state transitions in the neutron star low-mass X-ray binary 1RXS J180408.9–342058 during its 2015 outburst. We present results of the analysis of high-quality broad energy band (0.8–200 keV) data in three different spectral states: high/soft, low/very-hard, and transitional state. The broadband spectra can be described in general as the sum of thermal Comptonization and reflection due to illumination of an optically thick accretion disk. During the high/soft state, blackbody emission is generated from the accretion disk and the surface of the neutron star. This emission, measured at a temperature of $kT_{\text{bb}} \sim 1.2$ keV, is then Comptonized by a thick corona with an electron temperature of ~ 2.5 keV. For the transitional and low/very-hard state, the spectra are successfully explained with emission from a double Comptonizing corona. The first component is described by thermal Comptonization of seed disk/neutron star photons ($kT_{\text{bb}} \sim 1.2$ keV) by a cold corona cloud with $kT_e \sim 8$ –10 keV, while the second one originates from lower temperature blackbody photons ($kT_{\text{bb}} \leq 0.1$ keV) Comptonized by a hot corona ($kT_e \sim 35$ keV). Finally, from *NuSTAR* observations, there is evidence that the source is a new *clocked* burster. The average time between two successive X-ray bursts corresponds to ~ 7.9 and ~ 4.0 ks when the persistent emission decreases by a factor of ~ 2 , moving from a very hard to transitional state. The accretion rate ($\sim 4 \times 10^{-9} M_{\odot} \text{ yr}^{-1}$) and the decay time of the X-ray bursts longer than ~ 30 s suggest that the thermonuclear emission is due to mixed H/He burning triggered by thermally unstable He ignition.

Unified Astronomy Thesaurus concepts: [Binary stars \(154\)](#); [Low-mass X-ray binary stars \(939\)](#); [X-ray astronomy \(1810\)](#); [Gamma-ray bursters \(1878\)](#); [Gamma-ray astronomy \(628\)](#)

1. Introduction

Low-mass X-ray binaries (LMXB) are double star systems consisting of a low-mass object in orbit around a black hole or neutron star. When emission from an X-ray burst is observed the compact object can immediately be classified as a neutron star (NS). According to our present understanding, the X-ray emission in X-ray bursters comes from the release of gravitational potential energy from accretion processes onto the neutron star. The X-ray spectra are generally described as the sum of a soft thermal component originating from the accretion disk and/or neutron star surface, a hard X-ray component arising from inverse Compton scattering of soft thermal photons in a hot electron corona and a reflection component originated from the scattering of the Comptonized photons by the surface of the accretion disk. The emission of NS LMXBs shows two spectral states. In the high/soft state the disk is generally thought to extend down to the neutron star and it is responsible for the thermal emission, with the disk and neutron star being the source of the soft seed photons for Comptonization in the coronal region. In the low/hard state, the disk is believed to recede from a neutron star resulting in a weakened thermal component while the inner parts of a hot accretion flow produce hard X-ray emission. The spectral transitions are accompanied by luminosity variations and are generally explained in the framework of this truncated accretion disk model (see Done et al. 2007). In the low/hard state, the neutron star surface and disk emission are much weaker than in the high/soft state and the inner cavity of the

accretion disk could be replaced by a hot geometrically thick accretion flow. Comptonization of the corona electrons interacting with the soft photons from disk/neutron star and/or from photons internally generated by synchrotron of the coronal electrons produce hard X-ray emission (Veledina et al. 2013). In both spectral states the disk receives photons from the corona and produces the reflection and reprocessing features. The truncated disk scenario explains qualitatively many of the observed properties of X-ray binaries. However, the geometry and nature of the corona in all spectral states are still uncertain. X-ray emission may arise from different regions or from different physical processes, such as a multizone structure with an inhomogeneous hot accretion flow (Veledina et al. 2013) or a jet contributing to high energy emission (Markoff et al. 2005), although at X-ray wavelengths the jet emission is unlikely to be dominant (Malzac et al. 2009). Recently, there have been many attempts to accurately derive information on the innermost region surrounding NSs in LMXBs, such as the physical properties of the emission region of the reflection components and the geometry of the system. The use of broadband spectra together with improved methods for self-consistent spectral modeling to simultaneously fit the iron line profile and the Compton hump have proved to be a useful tool in this framework (Chiang et al. 2016; Di Salvo et al. 2019). In particular, the inferred values for the reflection amplitude give important information about the geometry of the emission region. In general, low values for the reflection amplitude have been found for NS LMXBs, lying between 0.2 and 0.3 (Di Salvo et al. 2015; Pintore et al. 2015; Matranga et al. 2017a, 2017b), where a value of 0.3 is indicative of a spherical corona (Matranga et al. 2017a). In some cases, even smaller

³ Einstein Fellow.

reflection fractions are observed. For example, Mazzola et al. (2019) reported a reflection amplitude of 0.05 in the *XMM-Newton* and *INTEGRAL* spectra of 4U 1702–49, which could indicate a different geometry with respect to a spherical corona (but see also the analysis of Iaria et al. 2016).

1RXS J180408.9–342058 was first detected in 1990 by the *ROSAT* satellite (Voges et al. 1999) and underwent a faint outburst in 2012 that was caught by *INTEGRAL* and *SWIFT* (Chenevez et al. 2012). During *INTEGRAL* Galactic Bulge monitoring observations, JEM-X instruments detected a Type-I thermonuclear burst which classified the compact object in this system as a neutron star. Assuming that this burst was Eddington limited, Chenevez et al. (2012) determined an upper limit on its distance to be $d \leq 5.8$ kpc. Follow-up *SWIFT* observations revealed that 1RXS J180408.9–342058 returned to quiescence (Kaur & Heinke 2012) and it remained until 2015 January 20, when both *SWIFT*/BAT and *MAXI*/GSC detected a new outburst (Krimm et al. 2015a, 2015b; Negoro et al. 2015). *INTEGRAL* observations of the Galactic center on 2015 February 16–17 detected this source in a hard state, with emission up to 100 keV (Boissay et al. 2015). The X-ray spectrum was described by a simple absorbed power-law model with a photon index of $\Gamma \sim 1.1$ (Degenaar et al. 2015).

On April 3, the hard X-ray flux dropped and the soft X-ray emission increased, indicating a transition from a low/hard to high/soft state (Degenaar et al. 2015). Baglio et al. (2016) reported on a detailed NIR/optical/UV study of 1RXS J180408.9–342058 during both the low/hard state (MJD 57,079) and high/soft state (MJD 57,136). The optical spectrum showed He I emission lines with a lack of H emission lines that are typically observed in LMXBs, suggesting an ultra-compact nature for this transient source. By combining the mass accretion rate with theoretical evolutionary tracks for a He white dwarf, Baglio et al. (2016) reported on a tentative orbital period of ~ 40 minutes. Based on the multiwavelength information, Degenaar et al. (2016) concluded that orbital periods of ~ 1 –3 hr are not ruled out. Furthermore, Baglio et al. (2016) studied the spectral energy distribution evolution, showing the emission was consistent with a simple thermal component during the soft state, while the presence of a tail in the NIR in addition to the thermal component during the hard state likely indicated a transient jet.

Detailed studies of the very hard and soft states of 1RXS J180408.9–342058 were performed with *NuSTAR* observations performed during the 2015 outburst (Degenaar et al. 2016; Ludlam et al. 2016). Ludlam et al. (2016) reported on the source in the very hard spectral state, showing multiple reflection features (Fe K_{α} detected with *NuSTAR*; N VII, O VII, and O VIII detected with *XMM-Newton*/RGS) from different ionization zones. Using relativistic reflection models they measured an inner disk radius ≤ 22.2 km and an inclination of the system between 18° and 29° . Degenaar et al. (2016) presented *NuSTAR*, *SWIFT*, and *Chandra* observations obtained around the peak brightness of this outburst ($L_{0.5-10 \text{ keV}} \simeq (2-3) \times 10^{37} (D/5.8 \text{ kpc})^2 \text{ erg s}^{-1}$) while the source was in the soft spectral state. The *NuSTAR* data still showed a relativistically broadened Fe K emission line that indicated that the inner edge of the accretion disk extended down to ~ 11 –17 km from the neutron star. Additionally, the inclination inferred from reflection modeling ($i \simeq 27^{\circ}$ – 35°) agreed with the results obtained while the source was in the hard spectral state.

From all *SWIFT* XRT observations obtained during the 2015 outburst of 1RXS J180408.9–342058, Parikh et al. (2017) found that during the low/hard state this source showed a photon index of $\Gamma \sim 1$. This is significantly lower than typical values of $\Gamma = 1.5$ – 2.0 for such systems in the hard state. The mechanism for producing such a hard spectrum remained unclear. Wijnands et al. (2017) used two *XMM-Newton* observations to study the rapid variability properties of 1RXS J180408.9–342058: one obtained early during the outburst in March 6 (see also Ludlam et al. 2016) and one just before the transition to the soft state on April 1. These authors reported the source exhibited an unusually strong noise component, particularly during the first *XMM-Newton* observation. At X-ray luminosities similar to those observed in 1RXS J180408.9–342058, they showed its timing properties are different with respect to what are commonly observed in the canonical hard state of a neutron star.

Parikh et al. (2017) reported on the *SWIFT* and *XMM-Newton* observations while the source was in the quiescence state. The X-ray spectra were dominated by a thermal component arising from the stellar surface temperature that decayed after the end of the outburst. Good spectral fits were obtained from these data by adding a power-law component in addition to the existing thermal emission. The power-law contributed 30% of the total unabsorbed flux in the 0.5–10 keV energy range. The origin of this component is unknown.

Recently, Gusinskaia et al. (2017) presented an EVLA monitoring study of the source through the 2015 outburst and back to quiescence for a total of six epochs. The enhanced sensitivity of the EVLA allowed them to follow the evolution of the radio counterpart at X-band (8–12 GHz) from the very hard X-ray state ($232 \pm 4 \mu\text{Jy}$) down to the soft X-ray state ($19 \pm 4 \mu\text{Jy}$). When the source faded to quiescence, a flux density upper limit of $\leq 13 \mu\text{Jy}$ was measured. Moreover, the wide bandwidth of the EVLA allowed them to perform a spectral analysis, resulting in a positive spectral index (0.12 ± 0.18) during the very hard state. The positive spectral index implied that the emission came from an optically thick jet, which agreed with the expectations for sources in hard X-ray states. However, the larger uncertainties of the soft-state measurements did not allow a proper estimation of the spectral index. Thus, they were not able to discern a change from optically thick to optically thin emission. These radio observations were performed with the EVLA in B and BnA configurations and resulted in an angular resolution of $1''.25$ and $0''.6$, respectively. As a result, the source was resolved from the nearby extended radio galaxy NVSS J180414342238 (Condon et al. 1998). Previous NVSS observations of this region, with an angular resolution of $45''$, would not have allowed a clear detection despite the possible presence of a very hard state. Gusinskaia et al. (2017) conclude that the weak radio emission seen in the soft state could still be residual emission from the very hard state, thus jet quenching could be even deeper than what was measured (more than one order of magnitude).

2. Observations and Data Analysis

To understand the spectral and timing properties of 1RXS J180408.9–342058 we analyze the quasi-simultaneous data in a homogeneous manner over a very broad energy band (0.8–200 keV). We report in Table 1 the observation log of the source performed with *INTEGRAL*/IBIS (Winkler et al. 2003),

Table 1
Observation Log

#	Instrument	Start Date (UTC)	Duration (ks)
1	<i>INTEGRAL</i> /IBIS	2015 Feb 16 12:34:50	5929.9
2	<i>Swift</i> /XRT	2015 Feb 17 17:21:58	0.960
3		2015 Feb 24 05:58:59	1.982
4		2015 Feb 26 02:27:59	1.848
5		2015 Feb 28 09:00:59	0.555
6		2015 Mar 2 21:32:06	1.099
7		2015 Mar 4 15:05:59	2.169
8		2015 Mar 9 02:04:59	1.734
9		2015 Mar 10 13:26:59	1.489
10		2015 Mar 13 00:11:59	0.595
11		2015 Mar 16 06:45:59	0.980
12		2015 Mar 23 06:12:52	0.200
13		2015 Mar 24 22:33:58	0.590
14		2015 Apr 1 16:52:59	1.858
15		2015 Apr 14 13:00:13	1.000
16		2015 Apr 15 09:46:59	1.839
17	<i>NuSTAR</i> /(FPMA,FPMB)	2015 Mar 5 09:21:07	80.096
18		2015 Apr 1 16:16:07	56.996
19		2015 Apr 14 12:11:07	45.596

SWIFT/XRT (Gehrels et al. 2004), and *NuSTAR*/FPMA-FPMB (Harrison et al. 2013) instruments.

The *INTEGRAL*/IBIS (Ubertini et al. 2003) data are processed using the standard Off-line Scientific Analysis (OSA v10.2) software released by the *INTEGRAL* Scientific Data Centre (Courvoisier et al. 2003).

The *SWIFT*/XRT (Barrow et al. 2005) data are processed using standard tools incorporated in HEASOFT (v6.19). Observations were taken in windowed timing mode. We used a box region with a length of $70''$ to extract source events and another region of the CCD away from the source for background events. When the XRT count rate was $>100\text{ c s}^{-1}$ we used a box-box region with a length of $70''$ and an exclusion of the inner of $2''$ to avoid pile-up effect (following the procedure in Romano et al. 2006).

The *NuSTAR*/FPMA and FPMB instruments data are processed following standard analysis, performed with NUSTARDAS included in HEASOFT (v.6.19). We used NUPRODUCTS to create light curves and spectra for the FPMA and FPMB, considering a circular region with a radius of $60''$ to extract source events and a region of the same size away from the source to extract background events.

For spectral fitting of each spectral state, we allow a constant to be free with respect to the FPMA data, for IBIS, XRT, and FPMB instruments. We use XSPEC v. 12.9.0n and data available in the following energy range: 0.8–9.0 keV for *SWIFT*/XRT, 3.5–50.0 keV for *NuSTAR*/FPMA and FPMB, and 22.0–200.0 keV for *INTEGRAL*/IBIS instrument. The *SWIFT*/XRT data below 0.8 keV are not included because *XMM-Newton*/RGS observations showed multiple emission lines (N VII, O VII, and O VIII), which cannot be resolved using the XRT data.

3. Results

This work reports on all three spectral states in a broad energy range (0.8–200.0 keV) and, in particular, the only data set that has high-quality broadband X-ray data available in the peculiar spectral/timing state, i.e., the so-called very hard

state by Parikh et al. (2017) and Wijnands et al. (2017). Both the persistent and X-ray burst emission have been analyzed in this work. To study the persistent emission, we extracted *INTEGRAL*/IBIS, *SWIFT*/XRT, *NuSTAR*/FPMA and *NuSTAR*/FPMB light curves and spectra excluding the times of Type-I X-ray bursts as reported in Section 3.1. Timing and spectral analysis of the Type-I X-ray bursts is in Section 3.2.

3.1. The Persistent Emission

Figure 1 (top panel) shows the IBIS light curve in the 23–50 keV energy band from 2015 February 16 (57,069 MJD) to 2015 April (57,137 MJD). This chosen energy range (0.8–200 keV) is the one that best represents the X-ray emission simultaneously in both the soft and hard states. From the beginning of the observation up to $\sim 57,110$ MJD the source was in a very hard X-ray state ($F_{23-50\text{ keV}} \sim 10^{-9}\text{ erg cm}^{-2}\text{ s}^{-1}$). Starting from $\sim 57,114$ MJD, 1RXS J180408.9–342058 entered into a transitional state as it passed from the very hard to the soft state. It stayed in the soft state up to the end of the *INTEGRAL* observation ($F_{23-50\text{ keV}} \sim 2 \times 10^{-11}\text{ erg cm}^{-2}\text{ s}^{-1}$) during the time interval 57,116–57,137 MJD. The middle panel of Figure 1 reports on the XRT light curve in the 0.5–10 keV energy band showing a gradual increase of the soft X-ray emission, confirming the transition of the source from the hard to the soft spectral state. The bottom panel of Figure 1 shows the FPMA light curve in the 3.5–50 keV energy band. *NuSTAR* has observed this source on three occasions: the first during the very hard state, the second during the transitional state, and the third when the source moved to the soft state.

Simultaneous data from three high energy instruments allow for the spectral evolution to be followed during the state transitions over a very broad energy band. To this aim we study the spectral behavior in a uniform manner separately for three different states:

1. Very hard state: the *INTEGRAL*, *SWIFT*, and *NuSTAR* observations performed between MJD 57,069 and MJD 57,110.
2. Transitional state: the *INTEGRAL*, *SWIFT*, and *NuSTAR* observations performed on MJD 57,114.
3. Soft state: the *INTEGRAL*, *SWIFT*, and *NuSTAR* observations performed between MJD 57,116 and MJD 57,137.

Previous analyses of the *NuSTAR* data (Degenaar et al. 2016; Ludlam et al. 2016) showed a complex spectrum from the steady emission during two spectral states (very hard and soft) consisting of Comptonization and reflection components with disk emission seen in the soft state only. High-quality data from transitional state are published in this work for the first time, but see also Marino et al. (2019).

3.1.1. The Very Hard State

To build the average broad energy band spectrum (0.8–200.0 keV) for a very hard state, we use the *NuSTAR* data mentioned above, the average spectrum with the combined *SWIFT* observations from 2 to 13 (see Table 1), and the *INTEGRAL* data. To fit these data we use the self-consistent model for X-ray reflection for a cutoff power-law irradiating an accretion disk, modeled in XSPEC by RELXILL (Garcia et al. 2014). The RELXILL model parameters are as follows: the emissivity q_1 between R_{in} and R_{break} , the emissivity q_2 between

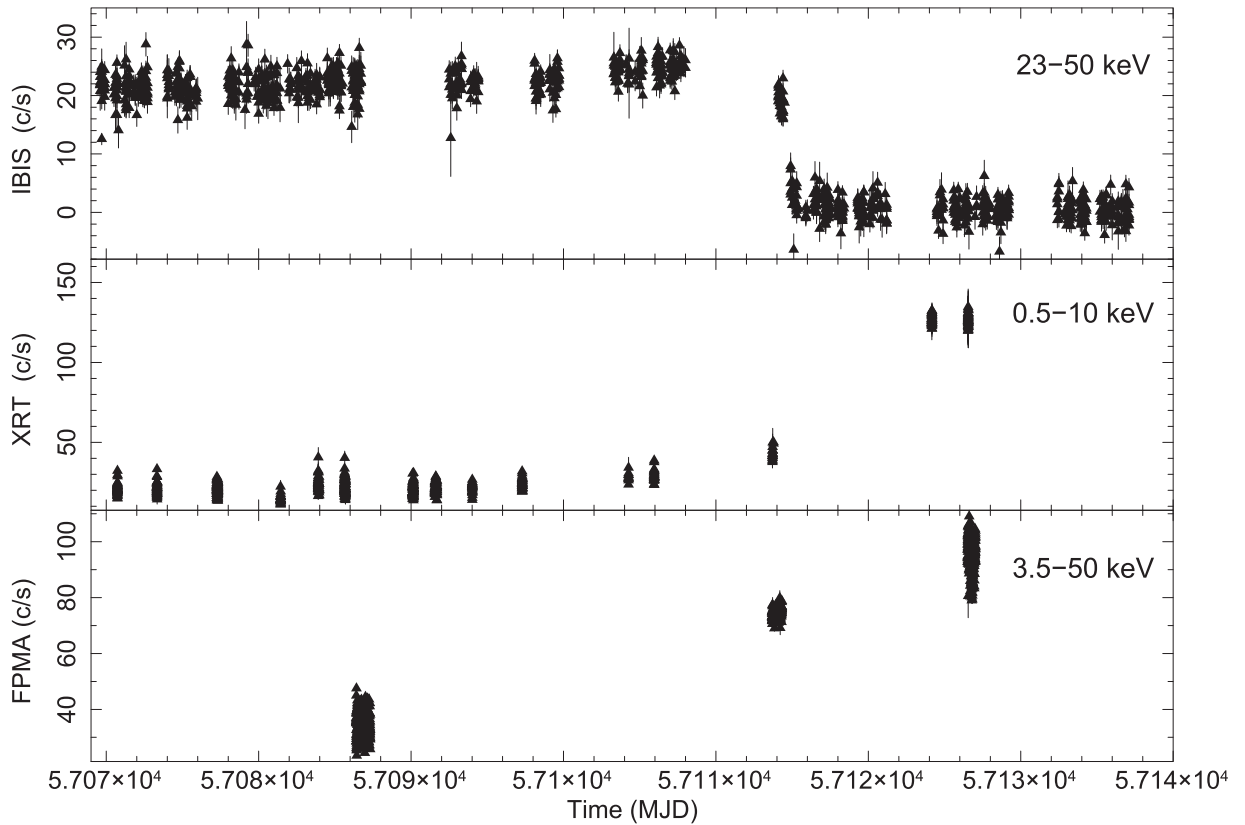


Figure 1. Top panel shows the IBIS light curve in the 23–50 keV energy band from 2015 February 16 (57,069 MJD) to 2015 April (57,137 MJD). Middle panel reports on the XRT light curve in the 0.5–10 keV energy band. The bottom panel shows the FPMA light curve in the 3.5–50 keV energy band.

R_{break} and R_{out} , break radius between the two emissivities R_{break} , inner and outer radius of the accretion disk R_{in} , R_{out} , spin parameter a , inclination of the disk i , ionization of the accretion disk ξ , the iron abundance of the material in the accretion disk A_{Fe} , the high energy cutoff of the incident power law $E_{\text{cut-refl}}$, the reflection factor $refl_frac$, power-law index of the incident spectrum Γ and normalization N_{refl} .

We begin with fitting the spectrum using the model proposed by Ludlam et al. (2016), which works well in the range of 3.5–50 keV, with all physical parameters being free in the fit, except for the fixed parameters $a = 0$, $R_{\text{in}} = 1 R_{\text{ISCO}}$ and $R_{\text{out}} = 500 R_{\text{ISCO}}$. When including the *INTEGRAL* data covering energies up to 200 keV, this model gives a poor fit ($\chi^2_{\text{red}}(\text{dof}) = 1.36(3050)$). Figure 2 (top model) shows the residuals in the data with respect to the RELXILL model. Two broad features below 2 keV and near 100 keV can be seen. We try to add a thermal Comptonization component to the model and we obtain $\chi^2_{\text{red}}(\text{dof}) = 1.10(3046)$ with significant residuals at both soft and high energies with respect to this model, even though the addition of the Comptonized component provides a better overall fit (Figure 2, bottom panel). Using this model, the addition of a soft disk blackbody component does not improve the fit quality ($\chi^2_{\text{red}}(\text{dof}) = 1.10(3044)$). Furthermore, the best-fit parameters result in an unphysical blackbody temperature of ~ 5 keV.

Considering this and the behavior in the radio/IR band during the low/hard state (Baglio et al. 2016; Gusinskaia et al. 2017), we fit these data by adding a second emission component and its reflection. To obtain the physical parameters of the primary continuum we use the XILCONV model. This model takes into account Doppler and relativistic effects due to

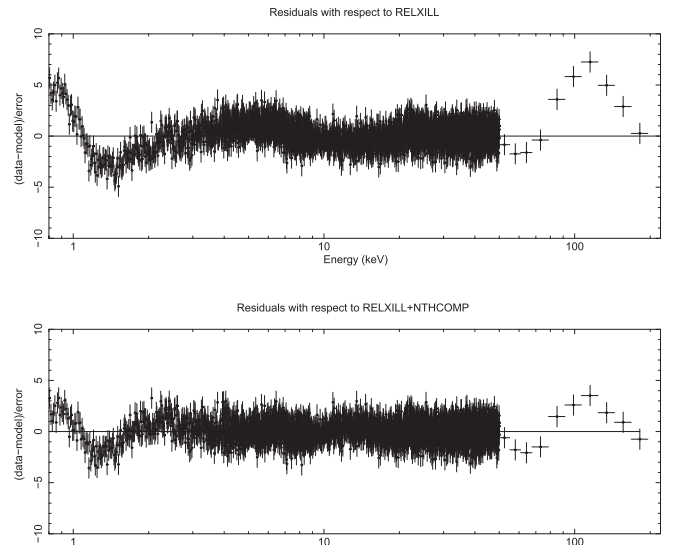


Figure 2. Residuals in units of sigma for the low/hard state spectra with respect to the model RELXILL (top panel) and RELXILL+NTHCOMP (bottom panel)

the fast motion of the matter in the disk, converting the XILLVER reflection table (which assumes a power law as illuminating spectrum) into a convolution for use with any continuum (Kolehmainen et al. 2011). It is parameterized by the reflection normalization $refl_frac$, the iron abundance of the material in the accretion disk A_{Fe} , the inclination of the disk i , ionization of the accretion disk ξ and exponential cutoff energy E_c . The reflection fraction is set to negative values so that the model only accounts for the reflection component. We report

Table 2
Results from Fitting *INTEGRAL*, *NuSTAR*, and *SWIFT* Spectral Data of the Persistent Emission

Parameter (unit)		Very Hard State	Transitional State	Soft State	
Exposure time XRT (s)		13170	1837	2813	
Exposure time FPMA (ks)		35.43	24.77	20.23	
Exposure time FPMB (ks)		35.56	25.00	20.51	
Exposure time IBIS (ks)		438.9	16.42	278.6	
Component	#	Parameter	Model 2	Model 2	Model 1
CONSTANT	1	C (FPMB)	1.004 ± 0.002	1.010 ± 0.008	0.996 ± 0.004
	2	C (XRT)	1.03 ± 0.05	0.91 ± 0.08	1.08 ± 0.04
	3	C (IBIS)	1.1 ± 0.5	1.2 ± 0.5	1.1 ± 0.2
TBABS	4	$N_{\text{H}} (\times 10^{22} \text{ cm}^{-2})$	0.3 ± 0.1	0.3 ± 0.2	0.3 ± 0.1
DISKBB	5	kT_{in} (keV)	1.15 ± 0.02
	6	$N_{\text{DISKBB}} (R_{\text{in}}^{\text{km}}/D_{10 \text{ kpc}})^2 \cos i$	21 ± 6
NTHCOMP	7	kT_{e} (keV)	10 ± 2	8 ± 2	2.50 ± 0.05
	8	kT_{bb} (keV)	$1.7^{+0.5}_{-0.3}$	1.7 ± 0.8	1.2 ± 0.2
	9	Γ	1.9 ± 0.2	1.9 ± 0.3	2.2 ± 0.2
	10	$N_{\text{nthcomp}} (\times 10^{-2})$	8 ± 2	12 ± 4	48 ± 10
RDBLUR	11	$Betor10$	-1.8 ± 0.8	-1.6 ± 1.5	-6 ± 5
	12	$R_{\text{in}} (R_{\text{G}})$	13^{+45}_{-8}	7^{+17}_{-2}	6 ± 1
	13	i ($^{\circ}$)	51^{+14}_{-18}	53^{+10}_{-28}	40 ± 16
XILCONV	14	$refl_frac$	≤ 0.2	0.3 ± 0.1	$0.9^{+1.0}_{-0.5}$
	15	$A_{\text{Fe}} (\times \text{Solar})$	0.5 ± 0.4	0.5 ± 0.4	0.8 ± 0.4
	16	$\log \xi$ (erg cm s^{-1})	1.3 ± 0.4	1.9 ± 0.6	$1.8^{+0.2}_{-1.5}$
NTHCOMP	17	kT_{e} (keV)	35 ± 8	34 ± 8	...
	18	kT_{bb} (keV)	≤ 0.1	≤ 0.1	...
	19	Γ	1.9 ± 0.2	1.7 ± 0.2	...
	20	$N_{\text{nthcomp}} (\times 10^{-2})$	3 ± 2	10 ± 3	...
RDBLUR	21	$Betor10$	$=\#11$	$=\#11$...
	22	$R_{\text{in}} (R_{\text{G}})$	$=\#12$	$=\#12$...
	23	i ($^{\circ}$)	$=\#13$	$=\#13$...
XILCONV	24	$refl_frac$	1.7 ± 0.5	0.4 ± 0.3	...
	25	$A_{\text{Fe}} (\times \text{Solar})$	$=\#15$	$=\#15$...
	26	$\log \xi$ (erg cm s^{-1})	1.8 ± 0.5	3.1 ± 0.8	...
$F_{0.8-200 \text{ keV}} (\times 10^{-10} \text{ erg cm}^{-2} \text{ s}^{-1})$		45 ± 13	55 ± 13	56 ± 5	
$L_{0.8-200 \text{ keV}} (\times 10^{37} \text{ erg s}^{-1})$		1.8 ± 0.6	2.2 ± 0.6	2.6 ± 0.2	
χ_{red}^2 (dof)		0.89 (3045)	0.90 (2633)	0.91 (1602)	

Note. We fixed $R_{\text{out}} = 500 R_{\text{ISCO}}$. All reflection fraction values are set to less than 0 to consider only the reflected component, we report the absolute value of this component for clarity. Fluxes are computed in the 0.8–200 keV energy range and they are unabsorbed fluxes. The luminosity is given assuming a distance of 5.8 kpc to the source. The constant multiplication factor was fixed to $C = 1$ for the *NuSTAR*/FPMA data and left free for the other instruments. Quoted errors reflect 1σ confidence levels.

the absolute value of this parameter in Table 2. To take into account the relativistic smearing effects in the inner region of the accretion disk, we use RDBLUR model, which is similar to DISKLINE (Fabian et al. 1989). This convolution model is parameterized by the index $Betor10$ of the power law, describing the emissivity, which scales as $r^{Betor10}$, the inner and outer radius R_{in} and R_{out} of the reflection region in units of gravitational radii (GM/c^2) and the inclination angle of the source i . To include a Comptonization component as the incident emission, we fit data with the following model:

1. CONST*TBABS*(NTHCOMP+RDBLUR*XIL-CONV*NTHCOMP) (Model 1)

In which the *inp_type* parameter was set to 1, indicating that the seed photons were emitted by the accretion disk. The outer radius was fixed at 500 gravitational radii ($R_g = GM/c^2$) as the fit was insensitive to its changes, the cutoff energy was fixed to be 2.7 times the temperature of the electrons (Eggen et al. 2013). All parameters in the NTHCOMP components were tied so that the resulting reflection emission is self-consistent with the illuminating continuum. Using Model 1, we obtain a poor fit ($\chi^2_{red}(\text{dof}) = 1.30(3051)$) with residuals showing distortion at low energy and strong residuals at high energies. We added a second thermal emission component NTHCOMP with its reflection as following:

1. CONST*TBABS*(NTHCOMP+RDBLUR*XIL-CONV*NTHCOMP+NTHCOMP+RDBLUR*XIL-CONV*NTHCOMP) (Model 2).

We link the index $Betor10$, inclination angle i , the inner and outer radius R_{in} and R_{out} and the iron abundance A_{Fe} of the first component to the same parameters of the second component. Conversely, we allow the ionization ξ , reflection *rel_frac* and normalization to change. This model improves the fit quality ($\chi^2_{red}(\text{dof}) = 0.89(3045)$). We add a soft disk blackbody component and we fit data with a model as

1. CONST*TBABS*(NTHCOMP+RDBLUR*XILCONV*NTHCOMP+NTHCOMP+RDBLUR*XILCONV*NTHCOMP+DISKBB) (Model 3).

Model 3 did not result in a substantial improvement in the fit of the data ($\chi^2_{red}(\text{dof}) = 0.89(3043)$). The best-fit parameters obtained with Model 2 are listed in Table 2 for the very hard state. The spectrum and model residuals in units of sigma are shown in Figure 3 (top panel).

3.1.2. The Transitional State

During the transitional state, the hard X-ray flux $F_{23-50 \text{ keV}} \sim 10^{-9} \text{ erg cm}^{-2} \text{ s}^{-1}$ is similar to the flux during the very hard state. For this reason, we try to fit these data with the same procedure used for the very hard state spectra. In the broad energy range 0.8–100 keV the model proposed by Ludlam et al. (2016) with all physical parameters being free in the fit (with the exception of the aforementioned spin, inner disk radius, and outer disk radius) gives a poor fit ($\chi^2_{red}(\text{dof}) = 1.28(2627)$). Adding to the model of a thermal Comptonization component, the fit quality reduces to $\chi^2_{red}(\text{dof}) = 1.10(2623)$.

When we use Model 1 similar to the hard state, we obtain $\chi^2_{red}(\text{dof})$ of 1.5 (2639) while Model 2 well fits the transitional state data ($\chi^2_{red}(\text{dof}) = 0.90(2633)$). The DISKBB component

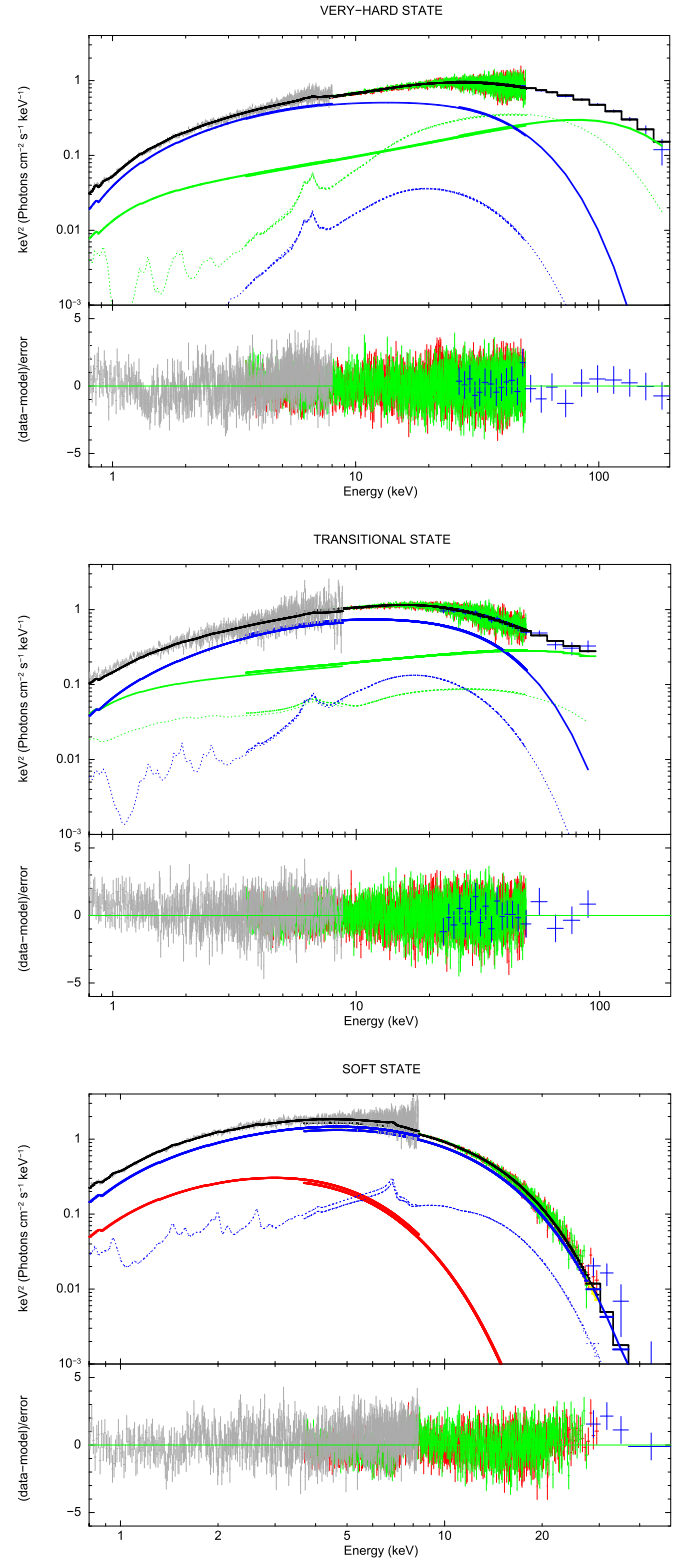


Figure 3. SWIFT/XRT, NuSTAR/FPMA and FPMB, and INTEGRAL/IBIS unfolded spectra and residuals in sigma rebinned for visual clarity for the very hard state (top panel), transitional state (middle panel), and high/soft state (bottom panel). Light gray points correspond to XRT data, red and green points correspond to FPMA and FPMB data, and blue points are IBIS data. For the very hard and transitional state we plot the spectral components of Model 2 and Model 1 for soft state. Red lines correspond to DISKBB components, blue lines to NTHCOMP components and its reflection component (blue dotted), green lines correspond to second NTHCOMP components and its reflection (green dotted).

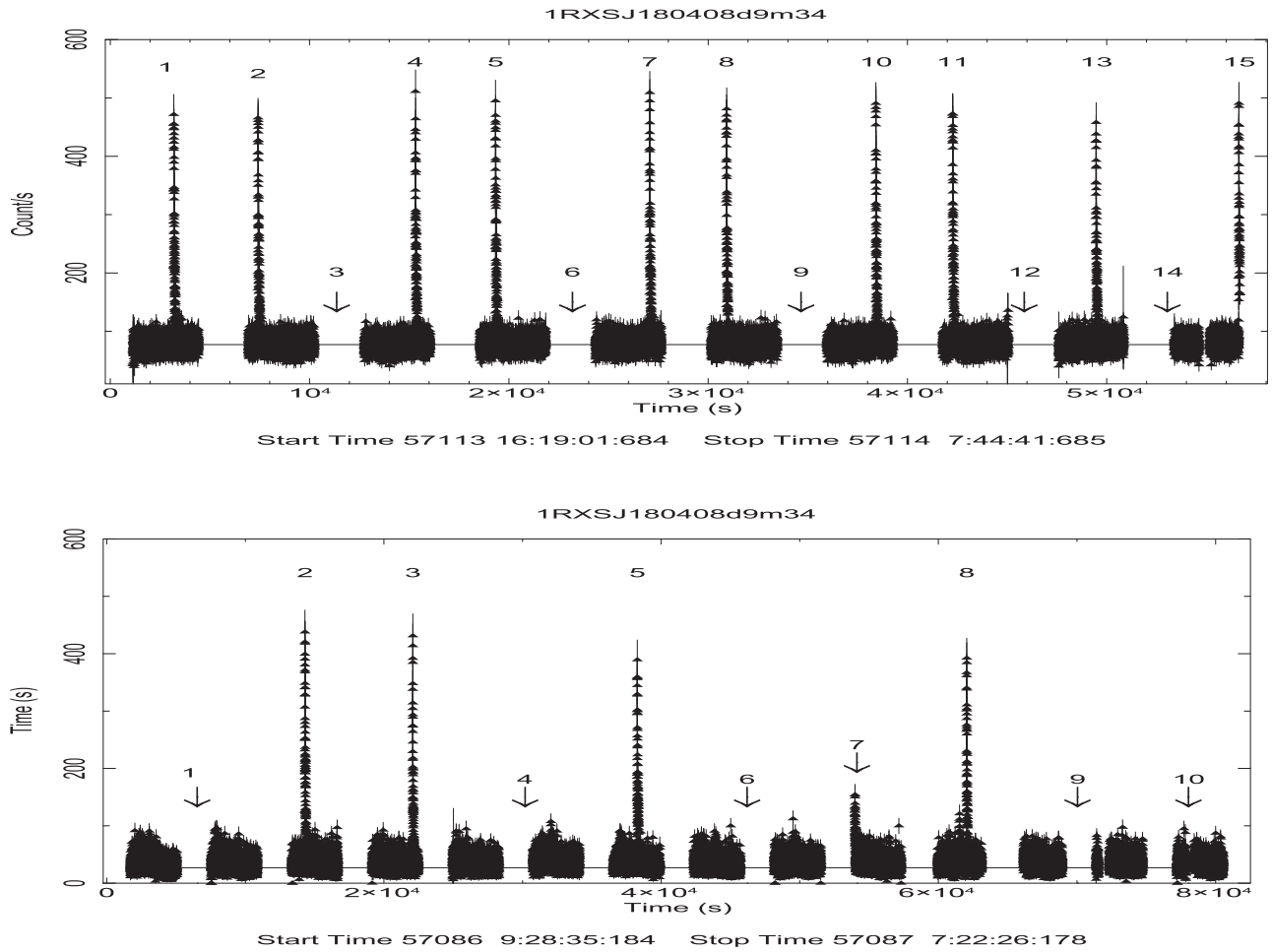


Figure 4. The 3.5–30 keV *NuSTAR* light curve in the transitional state during epoch number 2 (top) and in the hard state during epoch number 1 (bottom) using a bin size of 1 s.

is not required by the data ($\chi_{\text{red}}^2(\text{dof}) = 0.90(2631)$). The best-fit parameters are listed in Table 2 (Model 2) and the spectrum with residuals in sigma can be seen in the middle panel of Figure 3.

3.1.3. The Soft State

The *NuSTAR* observation in the soft state and the *SWIFT* observation number 15 (see Table 1) have previously been reported by Degenaar et al. (2016). The simplest model to describe these data consists of a thermal Comptonization component, a soft disk blackbody component, and a reflection component. To build an average broadband spectrum, we use the average *SWIFT*/*XRT* spectrum of the observation numbers 15 and 16 (see Table 1) and the *INTEGRAL* data extending the energy range up to ~ 50 keV. Similarly as proposed by Degenaar et al. (2016), we fit the broadband spectrum using a model including three emission components (a thermal Comptonization, a soft disk blackbody, and a model with reflection (CONSTANT*TBABS*(DISKBB+NTHCOMP+RELXILL) in XSPEC). All physical parameters are free in the fit with the exception of the following: $a = 0$, $R_{\text{in}} = 1 R_{\text{ISCO}}$, and $R_{\text{out}} = 400 R_{\text{ISCO}}$ (values from Degenaar et al. 2016). This model well describes the broadband 0.8–50.0 keV spectrum, with a $\chi_{\text{red}}^2(\text{dof}) = 0.83(1600)$. Taking into account that the single Comptonization component described the high/soft state data well and, in order to study the behavior of spectral parameters, we then fit these data also with Model 1,

similarly to what has been done for the hard and transitional states. The best-fit parameters are listed in Table 2 and the spectrum for the soft state with residuals with respect to the model are shown in Figure 3 (bottom panel).

3.2. The Type I X-Ray Bursts

We searched for the presence of timing signatures such as Type I X-ray bursts during the observations of 1RXSJ180408.9–342058. These were detected in a quasi-periodic manner during the transitional state, when *NuSTAR* observed 1RXSJ180408.9–342058 for ~ 57 ks. The top panel of Figure 4 shows the light curve with a bin time of 1 s in the 3.5–30 keV energy range. The presence of 10 thermonuclear Type-I bursts can be seen clearly within the light curve (see also Wijnands et al. 2017). The light curve does not show any statistically significant intensity variations outside of the X-ray bursts. Unfortunately, there are no data from *INTEGRAL*/*JEM-X* or *SWIFT*/*XRT* during X-ray bursts detected with *NuSTAR* instruments. To analyze the morphological properties of these bursts, we modeled the burst shape with linear rise ($I = I_{\text{peak}}(t - T_{\text{start}})/(T_{\text{peak}} - T_{\text{start}})$, for $T_{\text{start}} \leq t \leq T_{\text{peak}}$) followed by an exponential decay ($I = I_{\text{peak}} e^{-(t - T_{\text{peak}})/\tau}$, for $T \geq T_{\text{peak}}$), adding a constant factor to take into account the persistent flux. In Table 3 we report the start time (T_{start}), peak time (T_{peak}), exponential decay time (τ), and peak intensity (in unit of c s^{-1}) of each X-ray burst. All the bursts show the same

Table 3
Results from Fitting *NuSTAR* Light Curve of Type-I X-Ray Bursts

Burst Number	T_{start} (s)	T_{peak} (s)	τ (s)	Peak Intensity (c s^{-1})																													
2nd epoch																																	
1	3179 ± 1	3187 ± 1	37.5 ± 0.3	387 ± 12																													
2	7409 ± 1	7418 ± 1	35.6 ± 1.3	391 ± 13																													
4	15307 ± 1	15317 ± 1	37.8 ± 1.4	358 ± 12																													
5	19324 ± 1	19332 ± 1	34.3 ± 1.2	402 ± 14																													
7	27061 ± 1	27069 ± 1	35.7 ± 1.1	381 ± 13																													
8	30914 ± 1	30921 ± 1	33.1 ± 1.2	397 ± 13																													
10	38406 ± 1	38415 ± 1	36.0 ± 1.4	373 ± 15																													
11	42264 ± 1	42272 ± 1	34.9 ± 1.3	396 ± 13																													
13	49458 ± 1	49467 ± 1	37.5 ± 1.4 </tr <tr> <td>15</td> <td>56622 ± 1</td> <td>56630 ± 1</td> <td>36.7 ± 2.7</td> <td>370 ± 17</td> </tr> <tr> <td colspan="5" style="text-align: center;">1st epoch</td> </tr> <tr> <td>2</td> <td>14293 ± 1</td> <td>14300 ± 1</td> <td>38 ± 2</td> <td>376 ± 15</td> </tr> <tr> <td>3</td> <td>22073 ± 1</td> <td>22081 ± 1</td> <td>28 ± 2</td> <td>322 ± 15</td> </tr> <tr> <td>5</td> <td>38269 ± 1</td> <td>38277 ± 1</td> <td>41 ± 2</td> <td>302 ± 13</td> </tr> <tr> <td>8</td> <td>62031 ± 1</td> <td>62040 ± 1</td> <td>31 ± 2</td> <td>328 ± 18</td> </tr>	15	56622 ± 1	56630 ± 1	36.7 ± 2.7	370 ± 17	1st epoch					2	14293 ± 1	14300 ± 1	38 ± 2	376 ± 15	3	22073 ± 1	22081 ± 1	28 ± 2	322 ± 15	5	38269 ± 1	38277 ± 1	41 ± 2	302 ± 13	8	62031 ± 1	62040 ± 1	31 ± 2	328 ± 18
15	56622 ± 1	56630 ± 1	36.7 ± 2.7	370 ± 17																													
1st epoch																																	
2	14293 ± 1	14300 ± 1	38 ± 2	376 ± 15																													
3	22073 ± 1	22081 ± 1	28 ± 2	322 ± 15																													
5	38269 ± 1	38277 ± 1	41 ± 2	302 ± 13																													
8	62031 ± 1	62040 ± 1	31 ± 2	328 ± 18																													

Note. The light curves were fit in the 3.5–30 keV energy range using a burst component model (linear rise followed by an exponential decay) for the second and first epochs. The burst numbers correspond to those in Figure 4. The constant factor is $C = 77.16 \pm 0.10 \text{ c s}^{-1}$ and the $\chi^2_{\text{red}} = 1.3$ (d.o.f = 44612) for the second epoch. These values are $C = 34 \pm 3 \text{ c s}^{-1}$ and the $\chi^2_{\text{red}} = 2.3$ (d.o.f = 32106) for the first epoch; this high value of χ^2 is due to the tail of the nonfitted burst number 7.

characteristics: a rise time between ~ 8 and ~ 11 s, an exponential decay time between ~ 33 and ~ 38 s, and a peak intensity between ~ 335 and $\sim 402 \text{ c s}^{-1}$. As an example we show in Figure 5 the shape of burst number 5 fit with a linear rise between T_{start} and T_{peak} and an exponential decay after the peak.

To study the spectral characteristics of the Type-I X-ray burst emission, we carried out a time resolved spectral analysis in the 3.5–20 keV energy range. We fit each time resolved burst spectrum using a blackbody model with the preburst emission subtracted as background. The selected times are marked with symbols (a)–(d) in Figure 5 (left panel). Spectral parameters are reported in Table 4 while the time resolved spectroscopic results are shown in Figure 5 (right panel).

From Figure 4 (top panel) it is clear that these X-ray bursts are appearing at regular intervals: for four subsequent events (between 1 and 2, 4 and 5, 7 and 8, 10 and 11 in the top panel of Figure 4) the average waiting time between the bursts is $3990 \pm 77 \text{ s}$ measured from the burst peak. For five bursts (2–4, 5–7, 8–10, 11–13, and 13–15 of top panel in Figure 4) the average waiting time is $7498 \pm 130 \text{ s}$, which is about twice the previous waiting time. Assuming the presence of *clocked* X-ray bursts (i.e., source showing repeated X-ray bursts at regular time intervals, see Ubertini et al. 1999), we compute the time in which intermediate bursts would have happened (time 3, 6, 9, 12, and 14 of top panel of Figure 4). We note that, unfortunately, these times occurred during the *NuSTAR* orbital data gaps.

The $\sim 41 \text{ ks}$ *XMM-Newton* light curve (Figure 3 of Wijnands et al. 2017), starting 4381 s after the *NuSTAR* observation (between burst number 1 and number 2 of Figure 4), showed 11

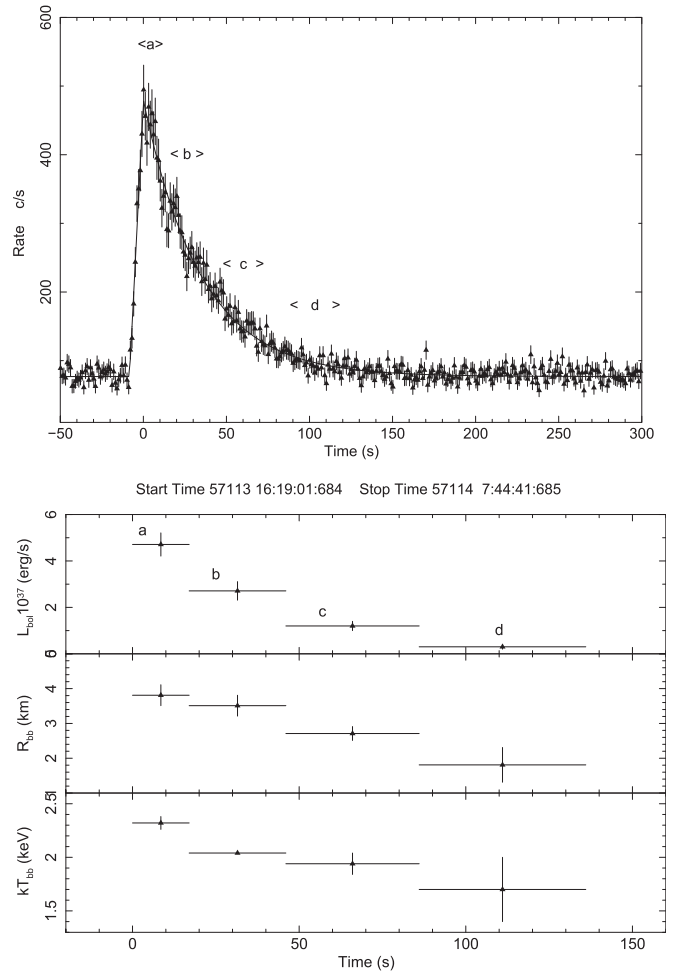


Figure 5. Top: profile of the X-ray burst number 5 (zoom of the Figure 4) in the 3.5–20 keV energy range with the model consisting of a linear rise followed by an exponential decay overlaid. Bottom: the change in luminosity, blackbody radius, and blackbody temperature (at 5.8 kpc) with time from the time resolved spectral fitting burst number 5. See Table 4 for parameter values.

consecutive Type I X-ray bursts every $\sim 3.7 \text{ ks}$, confirming the *clocked* burster behavior highlighted in the *NuSTAR* data.

During the very hard state, *NuSTAR* observed 1RXS J180408.9–342058 for $\sim 80 \text{ ks}$. The bottom panel of Figure 4 shows the light curve with a bin time of 1 s in the energy range of 3.5–30 keV. The light curve indicates the presence of four thermonuclear Type-I X-ray bursts (numbers 2, 3, 5, and 8). We model the light curves of these bursts in the same way as was done for the data in the transitional state. In Table 3 we report the start time (T_{start}), peak time (T_{peak}), exponential decay time (τ), and peak intensity (in unit of c s^{-1}) of each X-ray burst during this epoch. During this observation the X-ray bursts do not appear *clocked* as is evident in the transitional state. Moreover, the $\sim 57 \text{ ks}$ *XMM-Newton* light curve (Figure 3 of Wijnands et al. 2017), starting about five hours after the end of *NuSTAR* observation, showed 11 consecutive Type I X-ray bursts every $\sim 8.2 \text{ ks}$. We note that two consecutive Type-I X-ray bursts in the *NuSTAR* light curve (numbers 2 and 3 of the bottom panel of Figure 4) occurred with a waiting time of $7781 \pm 2 \text{ s}$. The X-ray burst numbers 5 and 8 occurred at about two and three times this value, respectively. Assuming the presence of *clocked* X-ray bursts, we compute the time in which bursts would have happened during the first *NuSTAR* observation (times 1, 4, 6, 7, 9, and 10 of bottom panel of Figure 4). As in the second epoch, these times

Table 4
Results from Fitting *NuSTAR* Spectral data of X-Ray Burst Number 5

Interval Time	Duration (s)	Constant (FPMB)	kT_{bb} (keV)	R_{bb} (km)	$L_{2-20\text{keV}}$ (10^{37}ergs^{-1})	χ^2_{ν} (dof)
a	17	1.0 ± 0.1	2.32 ± 0.06	3.8 ± 0.2	4.7 ± 0.5	125(137)
b	29	1.0 ± 0.1	2.03 ± 0.09	3.5 ± 0.3	2.7 ± 0.4	139(145)
c	40	1.0 ± 0.2	1.9 ± 0.1	2.7 ± 0.3	1.2 ± 0.2	174(174)
d	50	1.0 ± 0.2	1.7 ± 0.3	1.8 ± 0.3	0.3 ± 0.1	148(148)

Note. The data were modeled using a simple blackbody model during four time intervals. The shape of the burst profile can be seen in Figure 4. We assumed a distance of 5.8 kpc.

occurred during the *NuSTAR* orbital data gaps. The X-ray burst number 10 occurred during a short data gap due to good time interval. In the case of X-ray burst number 7, only a tail of the possible Type-I X-ray burst emission is detected due to an orbital data gap.

There were no Type-I X-ray bursts present in the data taken during the soft spectral state.

4. Discussion

4.1. Continuum Emission

The broadband analysis of 1RXS J180408.9–342058 indicates that the source moves from a low/hard state to a transitional state and then to a high/soft states. The X-ray luminosity accordingly increases from $L_{0.8-200\text{keV}} \simeq 1.8 \times 10^{37}\text{erg s}^{-1}$ to $L_{0.8-200\text{keV}} \simeq 2.6 \times 10^{37}\text{erg s}^{-1}$, assuming an intermediate value of $L_{0.8-200\text{keV}} \simeq 2.2 \times 10^{37}\text{erg s}^{-1}$ during the transitional state (for a distance of 5.8 kpc). When the source was in the very hard state, the *INTEGRAL*/*IBIS* data revealed a very hard emission that could not be fitted using a single Comptonization model. In order to properly describe the data, the spectra required two thermal Comptonization components, each with its own reflection component. The first thermal component is due to Comptonization of soft seed photons of temperature $\sim 1.7\text{keV}$ by a plasma with $kT_e \sim 10\text{keV}$. Its relativistic reflection component indicates that the inner disk is viewed at an inclination angle of $31^\circ\text{--}65^\circ$. The Fe abundance is $A_{\text{Fe}} \sim 0.5$ solar and the disk appears to be mildly ionized ($\log \xi \sim 1.3$). The reflection amplitude is lower than 0.2, indicating a relatively low illumination of the disk by the source of the primary Comptonization continuum. The second component is due to Comptonization of soft seed photons of temperature $\leq 0.1\text{keV}$ by a hot plasma with $kT_e \sim 35\text{keV}$. The reflection fraction is very high $\text{refl_frac} \sim 1.7$, indicating a slab-geometry for the corona, where all the thermal radiation must propagate through the corona prior to escaping from the system (Dove et al. 1997).

We estimate the optical depth τ of the Comptonizing region using the relation

$$\Gamma_{\text{comp}} = \left[\frac{9}{4} + \frac{1}{\tau \left(1 + \frac{\tau}{3}\right) \left(\frac{kT_e}{m_e c^2}\right)} \right]^{1/2} - \frac{1}{2}$$

(Zdziarski et al. 1996), where m_e and c are the electron mass and the speed of light, respectively, and the values of Γ_{comp} and kT_e are reported in Table 2. Assuming an optically thick corona and spherical emission, we calculate the emission radius of the seed photons $R_0 = 3 \times 10^4 d [f_{\text{Compton}} / (1 + y)]^{1/2} (kT_0)^{-2}$

(in units of kilometers), where d is the source distance in units of kiloparsecs, y is the Compton parameter $y = 4kT_e \max(\tau^2, \tau) / (m_e c^2)$ and kT_0 is the seed photon's temperature (in't Zand et al. 1999). We obtain an optical depth of $\tau \sim 5$ and a radius of the seed photon region of $R_0 \sim 2\text{km}$ for the first Comptonization component and $\tau \sim 2$ and $R_0 \sim 380\text{km}$ for the second Comptonization component. We consider the last value only indicative, with the spherical symmetry being disfavored by the high value of the reflection. These physical parameters indicate the presence of hot seed photons ($kT_{\text{bb}} \sim 1.7\text{keV}$) close to the neutron star surface ($R_0 \sim 2\text{km}$) which interact with a hot corona ($kT_e \sim 10\text{keV}$, $\tau \sim 5$). During the low/very-hard state, next to these standard components (blue lines in Figure 3) there is a second emission component (green lines in Figure 3) due to a hot corona ($kT_e \sim 35\text{keV}$, $\tau \sim 2$) interacting with cold ($kT_{\text{bb}} \leq 0.1\text{keV}$) seed photons located far from the neutron star ($R_0 \sim 380\text{km}$).

During the transitional state the spectral behavior is very similar to the low/hard state, with two Comptonization components. The first one with an electron temperature of $kT_e \sim 8\text{keV}$, a soft seed photon temperature of $\sim 1.7\text{keV}$, an optical depth of $\tau = 6$, and a seed radius of $R_0 \sim 2\text{km}$. Its relativistic reflection component indicates that the inner disk is viewed at an inclination angle of $25^\circ\text{--}63^\circ$. The Fe abundance is $A_{\text{Fe}} \sim 0.5$ solar and the ionization disk is $\log \xi \sim 1.9$. The reflection amplitude is ~ 0.3 indicating a value compatible with a spherical geometry of a compact corona inside an outer accretion disk. The second Comptonization component is due to a hot corona ($kT_e \sim 34\text{keV}$, $\tau \sim 3$) interacting with cold ($kT_{\text{bb}} \leq 0.1\text{keV}$) seed photons located farther out from the NS than the first component. Assuming a Shakura–Sunyaev disk, we can compute the distance from the central source where the temperature is expected to be $\sim 0.1\text{keV}$. Assuming that the observed $kT_{\text{bb}} \sim 1.7\text{keV}$ is the temperature at $R_c \sim 10\text{km}$, the relation $T(R) = [(3GM_{\text{NS}}\dot{M}/8\pi R^3\sigma) \times (1 - (R/R_c)^{1/2})]^{1/4}$ gives a distance of $\sim 400\text{km}$ for a disk location at a temperature of 0.1keV . This value is consistent with the radius of the region of the second seed photon population estimated in the previous paragraph, which could be compatible with the external part of the accretion disk.

When 1RXS J180408.9–342058 is in a high/soft state, the continuum from 0.7 to 50 keV is well described by a disk blackbody, a thermal Comptonization component, and its reflection. We obtain a hydrogen column density of $N_{\text{H}} = (0.3 \pm 0.1) \times 10^{22}\text{cm}^{-2}$ and an inner disk temperature of $kT_{\text{in}} \sim 1.2\text{keV}$. For the Comptonization component we obtain $\Gamma \sim 2.2$ and $kT_e \sim 2.5\text{keV}$. The relativistic reflection component indicates that the inner disk is viewed at an inclination angle of $24^\circ\text{--}56^\circ$. The Fe abundance is consistent with solar

composition ($A_{\text{Fe}} \sim 0.8$) and the disk appears to be mildly ionized ($\log \xi \sim 1.8$). The physical parameters are consistent with values obtained from the *NuSTAR* and *SWIFT* data reported by Degenaar et al. (2016), out of $N_{\text{H}} \sim 0.3$, $\Gamma \sim 2.2$, and $kT_e \sim 2.5$ keV. Small differences in column density and Γ can be explained by the different soft X-ray observations: the *SWIFT* spectrum reported here is an average of the observations (numbers 15 and 16 of Table 1) quasi-simultaneous with *INTEGRAL* data, where the data sample analyzed by Degenaar et al. (2016) includes observations performed after the *INTEGRAL* ones. Furthermore, the high energy *INTEGRAL* observations provided a better estimate of the electron temperature of the corona and indicate that the observed X-ray emission is dominated by thermal Comptonization with a Maxwellian electron distribution. Assuming a distance of 5.8 kpc and a correction factor of 1.7 (Shimura & Takahara 1995), the inner radius of the accretion disk is 9 ± 1 km. This value is consistent with the inner disk radius calculated from the RDBLUR model $R_{\text{in}} = 12 \pm 2$ km and with the expected radius of a neutron star, suggesting that the accretion disk was truncated near the stellar surface (Done et al. 2007).

Following the same procedure described for the low/hard state, we calculate an optical depth of $\tau \sim 10$ and a radius of the seed region $R_0 \sim 8$ km. Taking into account these physical parameters we can conclude that during the high/soft state the observed emission could be due to the seed photons from an accretion disk and/or neutron star surface and a thick electron corona ($\tau \sim 10$) with a temperature of ~ 2.5 keV. The position and temperature of the seed photons correspond to that of the disk photons.

During the high/soft state, a small fraction of the X-ray photons could be ascribed to jet emission, only detected when the thermal Comptonization is not dominating at high energies. However, the X-ray data presented here do not show any X-ray tail above ~ 50 keV.

In the low/hard state Baglio et al. (2016) reported IR/optical/UV emission from the jet simultaneous to the X-ray data presented here. In spite of this evidence, our data set is well fitted with a thermal Comptonization model that, in agreement with the energetic considerations of Malzac et al. (2009), favors a thermal model.

To verify whether the observed X-ray emission could be due to Comptonization of soft seed photons from a nonthermal electron population, we have fitted the data using a hybrid thermal/nonthermal model EQPAIR in XSPEC (Coppi 1999). In this model, the disk/corona system is a spherical hot plasma with the electrons illuminated by soft photons from the accretion disk. At low energies the electron distribution is Maxwellian, while at high energies this distribution is nonthermal. A fraction $l_{\text{nth}}/l_{\text{h}}$ of the power is ejected in the form of nonthermal electrons rather than contributing to the thermalized distribution (l_{th}). This model TBABS*(EQPAIR+DISKBB) gives a good fit $\chi_{\text{red}}^2(\text{dof}) = 1.1(1594)$ for the soft state, indicating a pure thermal emission $l_{\text{nth}}/l_{\text{h}} = 0$. During the transitional and very hard state this model gives a $\chi_{\text{red}}^2 > 1.4$ with significant residuals at high energies. Although the radio (Gusinskaia et al. 2017) and IR/optical/UV (Baglio et al. 2016) emission has been explained by the synchrotron radiation, the X-ray behavior favors a thermal Comptonization model to explain the high energy emission. At this stage, a small contribution from the nonthermal processes to the X-ray

flux cannot be ruled out, but it is not the dominant component in these spectral states.

The system shows two emission components with a different evolution from low/hard to high/soft state: the first one is a standard transition in the framework of the truncated disk model (blue lines in Figure 3), while the second one is a new component responsible for the peculiar very-hard emission (green lines in Figure 3). This peculiarity of the high energy behavior presented here is in agreement with the unusual very hard state observed by Parikh et al. (2017) in this source. They suggest that the source was not in a standard low/hard state, but rather in a new previously unrecognized state. They compare this spectral behavior with the standard low/hard state for LMXB at the same luminosity and report on the spectral and timing extreme properties: the hardness ratio of the spectra is significantly higher than the standard low/hard state spectra and the noise component in their power density spectra is stronger with very low typical frequencies (~ 0.01 Hz). Our analysis shows that this low/very-hard state is due to two Comptonization components.

Similar behavior was observed by D’Aí et al. (2007) at low accretion rates. They observe that a soft thermal emission from accretion disk and a thermal Comptonization component is unable to fit the broadband spectra of Sco X-1. Strong residuals in the high energy band required a power-law component, which could represent a second thermal Comptonization from a hot plasma or a hybrid thermal/nonthermal Comptonization. The main difference between the cases of Sco X-1 and 1RXS J180408.9–342058 is the presence of a high energy curvature ($kT_e \sim 35$ keV) in 1RXS J180408.9–342058 that makes thermal emission more plausible for this source.

A double Comptonization corona was also observed in 4U 1915–05 (but see also Gambino et al. 2019 for a different interpretation) and MAXI J0556–332 in the soft state (Sugizaki et al. 2013; Zhang et al. 2014), in GS 1826–238 in the low/hard state and in Aql X-1 in the low hard state just before it made a transition into the soft state (Ono et al. 2016). In the last two cases, the sources were at the highest luminosity end of the hard state ($L \sim 0.1 L_{\text{Edd}}$), at the same luminosity level as the very hard state of 1RXS J180408.9–342058. The GS 1826–238 spectrum was explained with an emission from a soft standard accretion disk Comptonized by a hot electron cloud and a blackbody emission Comptonized by another hotter electron corona. Strong similarities are found between those two sources: both are clocked bursters and require a double Comptonization component in their low/hard spectral states.

4.2. X-Ray Bursts

The thermonuclear instabilities on accreting neutron stars give information about the physical and chemical conditions of the binary system. In 1RXS J180408.9–342058, 10 Type-I X-ray bursts have been detected during the transitional state in the *NuSTAR* data, all showing the same spectral and timing characteristics. The chemical composition of the accreting material will influence the burst properties and can provide a tool to study the chemical composition. In fact, Type-I X-ray burst theory predicts four different regimes in mass accretion rate (\dot{M}) for unstable burning (Fujimoto et al. 1981; Fushiki & Lamb 1987 see also Bildsten 1998; Schatz et al. 1999; Bildsten & Ushomirsky 2000; Cooper & Narayan 2007; Peng et al. 2007). During the transitional state, the accretion rate was at $\sim 4 \times 10^{-9} M_{\odot} \text{ yr}^{-1}$, indicating that the X-ray bursts are due to

mixed H/He burning triggered by thermally unstable He ignition ($4\text{--}11 \times 10^{-10} M_{\odot} \text{ yr}^{-1} \lesssim \dot{M} \lesssim 2 \times 10^{-8} M_{\odot} \text{ yr}^{-1}$). The chemical composition can be experimentally confirmed through measurements of the burst duration. Whenever hydrogen is present in the burning material, the burst duration becomes longer with respect to the pure helium burning ($\tau \gtrsim 10$ s). This is due to the long series of β decays in the r-p process (see, e.g., Bildsten 1998; Bildsten & Ushomirsky 2000). During the very hard and transitional states, τ of the observed X-ray bursts is always longer than ~ 30 s, confirming the presence of the H in the burning.

1RXS J180408.9–342058 exhibits regular $\gtrsim 100$ s long Type-I X-ray bursts recurring at approximately periodic intervals of ~ 3.9 and ~ 7.9 ks between two successive X-ray bursts during the second and first epochs, respectively (see also Wijnands et al. 2017). Quasi-periodic bursting has been found in only three other sources: GS 1826-24 (Ubertini et al. 1999; Cocchi et al. 2000; Cornelisse et al. 2003; Galloway et al. 2004; Chenevez et al. 2016), GS 0836-429 (Aranzana et al. 2016) and EXO 1745-248 (Matranga et al. 2017b). Taking into account *NuSTAR* and *XMM-Newton* results (Wijnands et al. 2017) for 1RXS J180408.9–342058, the regular bursting regime has been observed during very hard and transitional states when the persistent count rate changes from $\sim 77 \text{ c s}^{-1}$ to $\sim 34 \text{ c s}^{-1}$. The burst frequency moves from ~ 7.9 to ~ 3.9 ks during these two regimes. The persistent luminosity ratio of ~ 2.3 is roughly similar to the waiting time ratio of ~ 2 . The correlation between the waiting time and accretion rate is expected by the standard burst model (see Fujimoto et al. 1981; Bildsten 1998), indicating that matter accretes on the neutron star surface in a very stable manner and Type-I X-ray burst occurs when enough material is accumulated to trigger the typical thermonuclear event.

No X-ray bursts have been observed in the soft state during the *NuSTAR*, *SWIFT*, and *INTEGRAL* observations. This is similar to the behavior observed for GS 1826-24 (Chenevez et al. 2016). The burst properties depend on the spectral states for these sources (Kajava et al. 2014; Kuuttila et al. 2017). Indeed, these authors show that the drivers of the bursting behavior are not only the accretion rate and chemical composition of the accreted material, but also the cooling that is linked to the spectral states.

5. Conclusions

We have analyzed the spectral evolution of 1RXS J180408.9–342058 in the 0.8–200 keV range during its 2015 outburst. The spectra are well described as the sum of thermal Comptonization and reflection due to illumination of the accretion disk. During the high/soft state, the blackbody component is due to thermal emission of the accreting disk peaking around 1.2 keV, plus an additional component indicating the Comptonization of disk/NS radiation by a population of electrons with a temperature of ~ 2.5 keV. Accordingly, during the low/very-hard and transitional states, the broadband spectra can be explained by two different components:

1. The first thermal Comptonization arises from hot seed photons ($kT_{\text{bb}} \sim 1.7$ keV) and a cold corona ($kT_e \sim 8\text{--}10$ keV) close to NS/accretion disk ($R_0 \sim 2$ km).
2. The second thermal Comptonization from cold seed photons ($kT_{\text{bb}} \leq 0.1$ keV) and a hot corona ($kT_e \sim 35$ keV) far from

the central region ($R_0 \sim 390$ km). This distance is the expected value for a disk temperature of 0.1 keV, suggesting that the seed photons come from the external part of the accretion disk.

The first thermal component indicates a standard transition from a high/soft state to low/hard state in the framework of the truncated disk (Done et al. 2007), while the second one explains the peculiar very-hard state.

Finally, *NuSTAR* observations show that this source is a new *clocked* burster with an average waiting time between two successive X-ray bursts of ~ 7.9 and ~ 4.0 ks when the persistent luminosity decreases by a factor of ~ 2 , moving from the very hard to the transitional state. The Type-I X-ray burst properties indicate that the thermonuclear emission is due to mixed H/He burning triggered by thermally unstable He ignition.

We thank Dr. N. Degenaar and J. van den Eijnden for suggestions and discussion, that improved our work.

We acknowledge the ASI financial/programmatic support via contracts ASI-INAF agreement number 2013-025.R1 and ASI-INAF 2017-14-H.0.

We acknowledge the use of public data from the *SWIFT* and *NuSTAR* data archive.

This research has made use of data provided by the High Energy Astrophysics Science Archive Research Center (HEASARC), which is a service of the Astrophysics Science Division at NASA/GSFC and the High Energy Astrophysics Division of the Smithsonian Astrophysical Observatory.

R.L. gratefully acknowledges funding through a NASA Earth and Space Sciences Fellowship and the support of NASA through Hubble Fellowship Program grant *HST-HF2-51440.001*.

F.O. acknowledges the support of the H2020 European HEMERA program, grant agreement No. 730970.

ORCID iDs

M. Fiocchi  <https://orcid.org/0000-0001-5697-6019>
 A. Bazzano  <https://orcid.org/0000-0002-2017-4396>
 G. Bruni  <https://orcid.org/0000-0002-5182-6289>
 R. Ludlam  <https://orcid.org/0000-0002-8961-939X>
 L. Natalucci  <https://orcid.org/0000-0002-6601-9543>

References

- Aranzana, E., Sánchez-Fernández, C., & Kuulkers, E. 2016, *A&A*, **586**, 12
 Baglio, M. C., D’Avanzo, P., Campana, S., et al. 2016, *A&A*, **587**, A102
 Barrow, D. N., Hill, J. E., Nausea, J. A., et al. 2005, *SSRv.*, **120**, 165
 Bildsten, L. 1998, *ASIC*, **515**, 419
 Bildsten, L., & Ushomirsky, G. 2000, *ApJ*, **529**, 33
 Boissay, R., Chenevez, J., Wilms, J., et al. 2015, *ATel*, **7096**, 1
 Chenevez, J., Galloway, D. K., in’t Zand, J. J. M., et al. 2016, *ApJ*, **818**, 135
 Chenevez, J., Kuulkers, E., Brandt, S., et al. 2012, *ATel*, **4050**, 1
 Chiang, C., Cackett, E. M., Miller, J. M., et al. 2016, *ApJ*, **821**, 105
 Cocchi, M., Bazzano, A., Natalucci, L., et al. 2000, in AIP Conf. Proc. 510, The Fifth Compton Symposium (Melville, NY: AIP), 203
 Condon, J. J., Cotton, W. D., Greisen, E. W., et al. 1998, *AJ*, **115**, 1693
 Cooper, R. L., & Narayan, R. 2007, *ApJ*, **661**, 468
 Coppi, P. S. 1999, in ASP Conf. Ser. 161, High Energy Processes in Accreting Black Holes, ed. J. Poutanen & R. Svensson (San Francisco, CA: ASP), 375
 Cornelisse, R., in’t Zand, J. J. M., Verbunt, F., et al. 2003, *A&A*, **405**, 1033
 Courvoisier, T. J. L., Walter, R., Beckmann, V., et al. 2003, *A&A*, **411**, 53C
 D’Aí, A., Życki, P., Di Salvo, T., et al. 2007, *ApJ*, **667**, 411
 Degenaar, N., Altamirano, D., Parker, M., et al. 2015, *ATel*, **7352**, 1
 Degenaar, N., Altamirano, D., Parker, M., et al. 2016, *MNRAS*, **461**, 4049

- Di Salvo, T., Iaria, R., Matranga, M., et al. 2015, *MNRAS*, **449**, 2794
- Di Salvo, T., Sanna, A., Burderi, L., et al. 2019, *MNRAS*, **483**, 767
- Done, C. M., Gierliński, & Kubota, A. 2007, *A&ARv*, **15**, 1
- Dove, J. B., Wilms, J., Maisack, M., & Begelman, M. C. 1997, *ApJ*, **487**, 759
- Egron, E., Di Salvo, T., Motta, S., et al. 2013, *A&A*, **550**, A5
- Fabian, A. C., Rees, M. J., Stella, L., & White, N. E. 1989, *MNRAS*, **238**, 729
- Fujimoto, M. Y., Hanawa, T., & Miyaji, S. 1981, *ApJ*, **247**, 267
- Fushiki, I., & Lamb, D. Q. 1987, *ApJ*, **323**, 55
- Galloway, D. K., Cumming, A., Kuulkers, E., et al. 2004, *ApJ*, **601**, 466
- Gambino, A. F., Iaria, R., Di Salvo, T., et al. 2019, *A&A*, **625**, A92
- Garcia, J., Dauser, T., Lohfink, A., et al. 2014, *ApJ*, **782**, 76
- Gehrels, N., Chincarini, G., Giommi, P., et al. 2004, *ApJ*, **611**, 1005
- Gusinskaia, N. V., Deller, A. T., Hessels, J. W. T., et al. 2017, *MNRAS*, **470**, 1871
- Harrison, F. A., Craig, W. W., Christensen, F. E., et al. 2013, *ApJ*, **770**, 103
- Iaria, R., Di Salvo, T., Del Santo, M., et al. 2016, *A&A*, **596**, A21
- in't Zand, J. J. M., Verbunt, F., Strohmayer, T. E., et al. 1999, *A&A*, **345**, 108
- Kajava, J. J. E., Nattila, J., Latvala, O., et al. 2014, *MNRAS*, **445**, 4218
- Kaur, R., & Heinke, C. 2012, *ATel*, **4085**, 1
- Kolehmainen, M., Done, C., & Diaz Trigo, M. 2011, *MNRAS*, **416**, 311
- Krimm, H. A., Barthelmy, S. D., Baumgartner, W., et al. 2015b, *ATel*, **6997**, 1
- Krimm, H. A., Kennea, J. A., Siegel, M. H., & Sbarufatti, B. 2015a, *ATel*, **7039**, 1
- Kuuttila, J., Kajava, J. J. E., Nattila, J., et al. 2017, *A&A*, **604**, 77
- Ludlam, R. M., Miller, J. M., Cackett, E. M., et al. 2016, *ApJ*, **824**, 37
- Malzac, Belmont, & Fabian 2009, *MNRAS*, **400**, 1512
- Marino, A., Del Santo, M., Cocchi, M., et al. 2019, *MNRAS*, **490**, 2003
- Markoff, S., Nowak, M. A., & Wilms, J. 2005, *ApJ*, **635**, 1203
- Matranga, M., Di Salvo, T., Iaria, R., et al. 2017a, *A&A*, **600**, A24
- Matranga, M., Papitto, A., Salvo, T. Di., et al. 2017b, *A&A*, **603**, A39
- Mazzola, S. M., Iaria, R., Di Salvo, T., et al. 2019, *A&A*, **621**, A89
- Negoro, H., Sugimoto, J., Mihara, T., et al. 2015, *ATel*, **7008**, 1
- Ono, K., Sakurai, S., Zhang, Z., Nakazawa, K., & Makishima, K. 2016, *PASJ*, **68**, 14
- Parikh, A., Wijnands, R., Degenaar, N., et al. 2017, *MNRAS*, **468**, 3979
- Peng, F., Brown, E. F., & Truran, J. W. 2007, *ApJ*, **654**, 1022
- Pintore, F., Di Salvo, T., Bozzo, E., et al. 2015, *MNRAS*, **450**, 2016
- Romano, P., Campana, S., Chincarini, G., et al. 2006, *A&A*, **456**, 917
- Schatz, H., Bildsten, L., Cumming, A., & Wiescher, M. 1999, *ApJ*, **524**, 1014
- Shimura, T., & Takahara, F. 1995, *ApJ*, **445**, 780
- Sugizaki, M., Yamaoka, K., Matsuoka, M., et al. 2013, *PAPS*, **65**, 58
- Ubertini, P., Bazzano, A., Cocchi, M., et al. 1999, *ApJ*, **514**, 27
- Ubertini, P., Di Cocco, G., Lebrun, F., et al. 2003, *A&A*, **411**, 131
- Veledina, A., Poutanen, J., & Vurm, I. 2013, *MNRAS*, **430**, 3196
- Voges, W., Aschenbach, B., Boller, Th., et al. 1999, *A&A*, **349**, 389
- Wijnands, R., Parikh, A. S., Altamirano, D., Homan, J., & Degenaar, N. 2017, *MNRAS*, **472**, 559
- Winkler, C., Courvoisier, T. J. L., Ci Cocco, G., et al. 2003, *A&A*, **411**, 1
- Zdziarski, A. A., Johnson, W. N., & Magdziarz, P. 1996, *MNRAS*, **283**, 193
- Zhang, Z., Makishima, K., Sakurai, S., et al. 2014, *PAPJ*, **66**, 120